

## MATERIALS SCIENCE

## Near-atomic-scale observation of grain boundaries in a layer-stacked two-dimensional polymer

Haoyuan Qi<sup>1,2,3\*</sup>, Hafeesudeen Sahabudeen<sup>2,3†</sup>, Baokun Liang<sup>1†</sup>, Miroslav Položij<sup>2</sup>, Matthew A. Addicoat<sup>4</sup>, Tatiana E. Gorelik<sup>1</sup>, Mike Hamsch<sup>3,5</sup>, Manuel Mundszinger<sup>1</sup>, SangWook Park<sup>2,3</sup>, Bettina V. Lotsch<sup>6,7</sup>, Stefan C. B. Mannsfeld<sup>3,5</sup>, Zhikun Zheng<sup>8</sup>, Renhao Dong<sup>2,3</sup>, Thomas Heine<sup>2,9,10\*</sup>, Xinliang Feng<sup>2,3\*</sup>, Ute Kaiser<sup>1\*</sup>

Two-dimensional (2D) polymers, hold great promise in the rational materials design tailored for next-generation applications. However, little is known about the grain boundaries in 2D polymers, not to mention their formation mechanisms and potential influences on the material's functionalities. Using aberration-corrected high-resolution transmission electron microscopy, we present a direct observation of the grain boundaries in a layer-stacked 2D polyimine with a resolution of 2.3 Å, shedding light on their formation mechanisms. We found that the polyimine growth followed a "birth-and-spread" mechanism. Antiphase boundaries implemented a self-correction to the missing-linker and missing-node defects, and tilt boundaries were formed via grain coalescence. Notably, we identified grain boundary reconstructions featuring closed rings at tilt boundaries. Quantum mechanical calculations revealed that boundary reconstruction is energetically allowed and can be generalized into different 2D polymer systems. We envisage that these results may open up the opportunity for future investigations on defect-property correlations in 2D polymers.

## INTRODUCTION

Since the discovery of graphene, two-dimensional (2D) materials have provided a fascinating playground for elucidating and advancing fundamental science (1). Because of their unique physical and chemical properties, inorganic 2D materials, such as graphene and transition metal dichalcogenides, hold great promise for next-generation applications (2). However, despite their outstanding intrinsic characteristics, post-synthetic treatment is often necessary to access the desired functionalities (3, 4). Therefore, exploring the promised land of rational design of 2D materials has become indispensable. Recent years have witnessed the rise of organic counterparts in the grand family of 2D materials, such as 2D polymers (5–10) and 2D covalent organic frameworks (COFs) (11–14). Because of the enormous chemical and structural diversity, synthetic 2D polymers can be tailored for potential applications in optoelectronics, sensing, catalysis, separation, and energy storage and conversion (15, 16).

Recently, vigorous efforts have been devoted to the synthesis of 2D polymers via different synthetic routes, among which, solid-state and solvothermal synthesis has afforded layer-stacked 2D

polymers in powder form (5, 6), and synthesis at air-water and liquid-liquid interfaces opened up the door to highly crystalline 2D polymer thin films with controllable crystallographic orientation and defined thickness (7–10). Note that, despite the remarkable advancements in synthetic chemistry, no crystal can be exempt from defects. For graphene and other inorganic 2D materials, local defects and grain boundaries (GBs) have been found to play a vital or even dominant role in the electronic, mechanical, and magnetic properties (17, 18). For 2D polymers, unfortunately, the understanding of the occurrence and nature of defects is still in its infancy, not to mention their formation mechanisms and potential influences on the material functionalities.

Aberration-corrected high-resolution transmission electron microscopy (AC-HRTEM) has been proven extremely powerful in elucidating spatially localized information down to atomic scale (19, 20). However, because of the strong interaction between hydrogen atoms and incident electrons, hydrogen-containing organic materials are extremely prone to structural disintegration under the electron beam (21). Therefore, only a few experiments have explored crystal defects in 2D polymers and 2D COFs. Recently, by converting an imine-linked 2D COF into an electron beam-resilient thiazole-linked COF, an HRTEM observation of defect sites and GBs has been reported (22). However, only the primary channels have been resolved, and the detailed molecular arrangements at GBs remain largely elusive because of the limited image resolution (i.e., 21.3 Å).

Here, by using AC-HRTEM imaging, we report a direct observation of GB structures in a layer-stacked 2D polyimine (L-2D-PI) with an unprecedented resolution of 2.3 Å. The unprocessed AC-HRTEM images are directly interpretable, allowing for reliable identification of nodes and linkers not only in the pristine molecular network but also at defect sites. We elucidate a broad spectrum of GB structures, including antiphase boundary (APB), low-angle GB (LAGB), high-angle GB (HAGB), and boundary reconstructions, down to near-atomic scale. Our results provide a comprehensive and unambiguous observation of GBs in a 2D polymer

Copyright © 2020 The Authors, some rights reserved; exclusive licensee American Association for the Advancement of Science. No claim to original U.S. Government Works. Distributed under a Creative Commons Attribution NonCommercial License 4.0 (CC BY-NC).

<sup>1</sup>Central Facility of Electron Microscopy, Electron Microscopy Group of Materials Science, Universität Ulm, 89081 Ulm, Germany. <sup>2</sup>Faculty of Chemistry and Food Chemistry, Technische Universität Dresden, 01062 Dresden, Germany. <sup>3</sup>Center for Advancing Electronics Dresden (cfaed), Technische Universität Dresden, 01062 Dresden, Germany. <sup>4</sup>School of Science and Technology, Nottingham Trent University, NG11 8NS Nottingham, UK. <sup>5</sup>Faculty of Electrical and Computer Engineering, Technische Universität Dresden, 01069 Dresden, Germany. <sup>6</sup>Max Planck Institute for Solid State Research, 70569 Stuttgart, Germany. <sup>7</sup>Department of Chemistry, Ludwig-Maximilians-Universität München, 81377 Munich, Germany. <sup>8</sup>Key Laboratory for Polymeric Composite and Functional Materials of Ministry of Education, Guangdong Engineering Technology Research Center for High-Performance Organic and Polymer Photoelectric Functional Films, School of Chemistry, Sun Yat-Sen University, 510275 Guangzhou, P.R. China. <sup>9</sup>Helmholtz Center Dresden-Rossendorf, Institute of Research Ecology, Leipzig Research Branch, 04318 Leipzig, Germany. <sup>10</sup>Department of Chemistry, Yonsei University, 03722 Seoul, Republic of Korea.

\*Corresponding author. Email: ute.kaiser@uni-ulm.de (U.K.); xinliang.feng@tu-dresden.de (X.F.); thomas.heine@tu-dresden.de (T.H.); haoyuan.qi@uni-ulm.de (H.Q.)

†These authors contributed equally to this work.

crystal, lending new insights into the GB formation mechanisms in 2D polymers.

## RESULTS AND DISCUSSION

### Synthesis and molecular structure of L-2D-PI

Figure 1A illustrates the synthesis of L-2D-PI at an air-water interface. The key to the synthesis is the application of a surfactant monolayer, which provides a confined 2D template for the polymerization (8, 9). First, a chloroform solution of sodium oleyl sulfate (SOS) was dropped onto the water surface. After the evaporation of chloroform, the SOS molecules self-assemble into a condensed monolayer with the anionic  $\text{SO}_4^-$  head groups pointing toward the water phase. Subsequently, an aqueous solution of 5,10,15,20-tetrakis(4-aminophenyl)-21*H*,23*H*-porphyrin (TAPP) protonated by triflic acid was injected into the water phase at 50°C. Because of the

hydrogen bonding and electrostatic interactions between the protonated TAPPs and  $\text{SO}_4^-$  head groups of SOS, the SOS monolayer locks TAPP into a face-on configuration (i.e., a necessary prerequisite for 2D polymerization). In the end, 2,5-dihydroxyterephthalaldehyde (DhTPA) was added into the water phase, which triggered the Schiff-base condensation of amino and aldehyde groups (Fig. 1B). The interfacial reaction was carried out at 50°C affording a continuous L-2D-PI thin film. A systematic study on the interfacial synthesis of L-2D-PI can be found elsewhere (23). The L-2D-PI film is readily transferrable onto  $\text{SiO}_2/\text{Si}$  substrates and TEM grids for subsequent characterizations. Atomic force microscopy (AFM) reveals a film thickness of ca. 40 nm. Imine bond formation is confirmed by Raman and Fourier transform infrared spectroscopy (fig. S1).

To probe the molecular structure of L-2D-PI, we performed electron diffraction on the freestanding film suspended on a hexagonal copper grid (Fig. 1C). Selected-area electron diffraction (SAED)

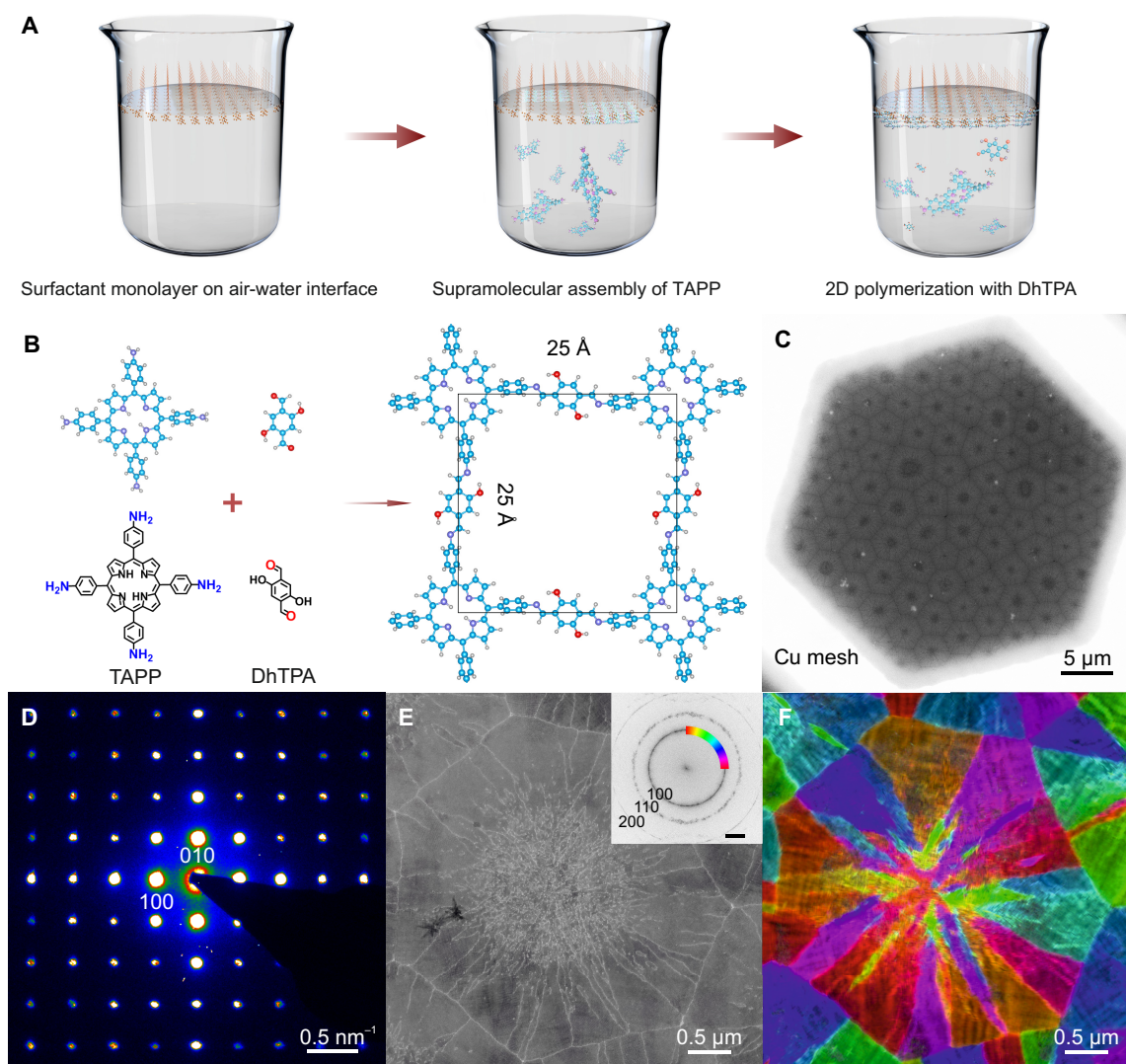


**Fig. 1. Synthesis, electron diffraction, and micromorphology of L-2D-PI.** (A) Schematic of the surfactant-assisted synthesis of L-2D-PI at an air-water interface. (B) Reaction scheme of Schiff-base condensation between TAPP and DhTPA (blue: C; purple: N; red: O; gray: H). (C) Scanning electron microscopy (SEM) image of the freestanding L-2D-PI thin film transferred onto a hexagonal copper mesh. (D) Selected-area electron diffraction (SAED) pattern. (E) Stitched TEM image. Inset: Fast Fourier transform (FFT) pattern of (E). Scale bar: 0.2 nm<sup>-1</sup>. The color-coded Fourier mask is overlaid. (F) Color-coded grain orientation map of (E) displaying “micro-flowers.” The triangular-shaped single-crystalline grains (“petals”) emanate from specific locations (“pistils”).

shows a square lattice with first-order reflections at  $0.4 \text{ nm}^{-1}$ , i.e.,  $25 \text{ \AA}$  (Fig. 1D). 3D nano-beam electron diffraction (NBED) yields a tetragonal lattice with  $a = b = 25 \text{ \AA}$  and  $c = 4 \text{ \AA}$ , which is further supported by the grazing-incidence wide-angle x-ray scattering (GIWAXS) measurement (figs. S2 and S3). As determined by density functional tight-binding (DFTB) calculations, the condensation of TAPP and DhTPA results in a square polyimine network with  $a = b = 25 \text{ \AA}$  (Fig. 1B), concurring with the diffraction data (figs. S2 and S3). The out-of-plane lattice parameter ( $4 \text{ \AA}$ ) is readily attributed to the interlayer  $\pi$ - $\pi$  stacking of L-2D-PI.

### Grain size, shape, and orientation

To examine the micromorphology of the L-2D-PI thin film, we acquired a stitched TEM image with the 200 fringe of the  $25\text{-\AA}$  unit cell resolved (Fig. 1E and fig. S4). Orientation-dependent Fourier filtering (Fig. 1E, inset) of the stitched image reveals the size, shape, and orientation of the grains, displaying “micro-flowers” on the thin film (Fig. 1F). We found no amorphous fragments within the probed area, demonstrating the high crystallinity of L-2D-PI.

The stitched image and its corresponding grain orientation map enabled a statistical analysis of grain sizes and tilt angles at GBs. The “pistils” contain stochastically oriented grains with an average size of  $(1.56 \pm 0.35) \times 10^{-3} \mu\text{m}^2$ , whereas those on the “petals” are one to three orders of magnitude larger, ranging from  $0.05$  to  $1.14 \mu\text{m}^2$ . Moreover, GBs formed by the misoriented grains exhibit no preferential tilt angles (fig. S4). These results have a twofold implication on the crystal growth process. First, the pistils are likely nucleation sites where the initial crystallites emerge under the surfactant molecules. Crystal growth could then proceed via the incorporation of building units, such as monomers, oligomers, etc., onto the crystallites, leading to a radial expansion of the micro-flowers until the surface coverage reaches unity (fig. S4). Note that the contour of the micro-flowers lies at the midpoint between two pistils (Fig. 1C), further rationalizing the “birth and spread” mechanism (24). As such, the formation of tilt GBs is attributed to the coalescence of stochastically oriented grains during growth. Similar phenomenon has been observed when crystallizing paraffin wax from the melt, where the crystallites expand independently until they come into contact. As a result, the GBs depend on the relative position of the neighboring crystallites rather than on the crystallographic system of the material (25).

### AC-HRTEM imaging of the molecular network with near-atomic resolution

The high crystallinity and abundance of GBs render L-2D-PI an ideal prototype for the investigation of boundary structures, provided that the molecular network can be imaged with sufficient resolution. Nowadays, aberration-corrected TEMs readily offer an instrumental resolution in sub-angstrom regime (20). Yet, hydrogen-containing organic materials are extremely prone to structural disintegration during HRTEM imaging (21), imposing severe limits on the achievable specimen resolution. Low-dose approach mitigates irradiation damage at the expense of reduced signal-to-noise ratio and image contrast, leading to poor object visibility (26). Therefore, the key to HRTEM imaging of 2D polymers lies in balancing electron dose (i.e., specimen resolution) and image contrast (vide infra).

To determine the correlation between specimen resolution [ $d_s$  ( $\text{\AA}$ )] and corresponding tolerance dose [ $D_t$  ( $e^-/\text{\AA}^2$ )], we performed a dose series analysis in diffraction mode and observed the fading of diffraction spots as a function of accumulated electron dose. The

intensity of each  $h00$  reflection decreases monotonically until reaching a plateau at a specific electron dose, at which we estimated the  $D_t$  for this reflection (fig. S5). The next question is, which  $d_s$  do we aim at? Note that the smaller the target  $d_s$  (i.e., higher resolution), the lower the  $D_t$ , and the finer the pixel size [ $p$  ( $\text{\AA}$ )] must be to resolve  $d_s$  on the charge-coupled device (CCD) camera. Consequently, the average number of electrons per pixel ( $e_p$ ) drops with  $e_p = D_t p^2$ , where  $p \leq d_s/2$ , reducing the signal-to-noise ratio in the image. A trade-off between  $d_s$  and object visibility is thus necessary. Because the width of the benzene ring in the smallest building block (i.e., DhTPA) is  $2.4 \text{ \AA}$ , we decided on a target  $d_s$  of  $2.3 \text{ \AA}$  (i.e.,  $4.4 \text{ nm}^{-1}$ ) to resolve both DhTPAs and TAPPs. Here, extra caution should be warranted when choosing the defocus value. Although high defocus substantially enhances image contrast under the same electron dose, the increased contrast delocalization may introduce “ghost molecules” at defect sites and GBs, incurring the risk of false interpretation (27, 28). Figure S6 presents the calculated contrast delocalization as a function of spatial frequency ( $q$ ) and defocus. For  $q = 4.4 \text{ nm}^{-1}$  (i.e., target resolution of  $2.3 \text{ \AA}$ ), the delocalization already amounts to half a unit cell ( $12.5 \text{ \AA}$ ) at a defocus of ca.  $-150 \text{ nm}$ . As demonstrated by HRTEM image simulation (fig. S6), further increase of the defocus leads to delocalized contrast in the primary channels and defect sites. In other words, in the raw HRTEM images, the contrast no longer straightforwardly correlates to the projected structure, complicating the direct image interpretation. Consequently, for reliable defect analysis in 2D polymers, it is desirable to precisely control the defocus during image acquisition.

To this end, we used an “in-focus” acquisition approach (see Materials and Methods). Because of the large lateral size and homogeneous thickness of the L-2D-PI film, we could fine-tune the defocus in the vicinity of the point of interest so as to avoid pre-exposure on the point of interest. Figure 2A shows an unprocessed AC-HRTEM image acquired with a defocus of ca.  $-100 \text{ nm}$  and an electron dose of  $100 e^-/\text{\AA}^2$ . The electron dose is  $20 e^-/\text{\AA}^2$  lower than the  $D_t$  of the target  $d_s$ . To maximize the signal-to-noise ratio, we selected a pixel size of  $1.15 \text{ \AA}$ , setting the Nyquist frequency exactly at  $2.3 \text{ \AA}$  (Fig. 2B). According to image simulation (Fig. 2, C and D), under the experimental conditions, the L-2D-PI network appears dark, and the primary channels appear bright. The image is free of imaging artifacts, and both TAPPs and DhTPAs are readily identifiable. Note that, under certain circumstances, such as limited lateral size and/or substantial variation in sample thickness, the implementation of in-focus acquisition becomes practically challenging, and images would have to be acquired with undefined defocus values, thus prone to imaging artifacts. In this case, the detrimental effects of delocalization can still be partially or even fully compensated (depending on the algorithm) via advanced contrast transfer function correction techniques (29, 30).

### GBs and their formation mechanisms

With the aforementioned experimental design, we examined the molecular structures of various GBs. Figure 3A presents an APB across which the upper domain is shifted by half a unit cell along [100] and [010] directions with respect to the lower one (i.e., displacement vector  $\mathbf{R} = 1/2 [110]$  in Fig. 3B). Figure 3C shows the formation and annihilation of an APB. Burgers circuit surrounding the defect region reveals two perfect dislocations with Burgers vectors of  $\mathbf{b} = [100]$  and  $\mathbf{b} = [010]$ , and each perfect dislocation is dissociated into two partials, i.e.

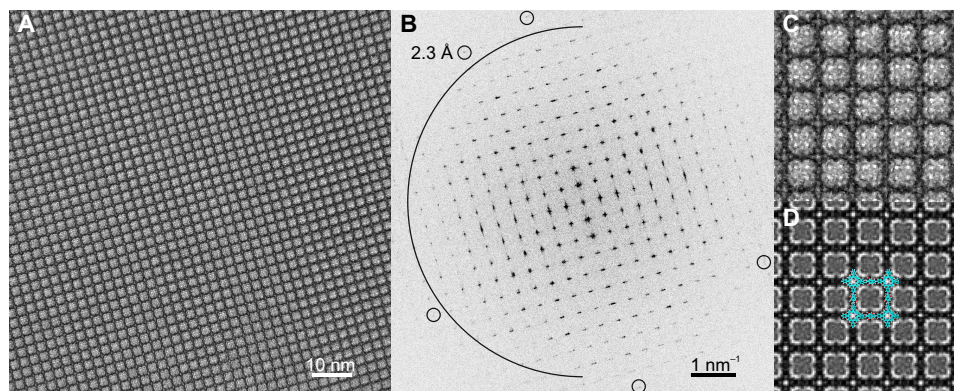


**Fig. 2. AC-HRTEM imaging of L-2D-PI.** (A) Unprocessed AC-HRTEM image of L-2D-PI. (B) FFT pattern of (A). The half-circle marks the spatial frequency of  $4 \text{ nm}^{-1}$  (i.e.,  $2.5 \text{ \AA}$ ). The small circles mark the reflections at Nyquist frequency  $4.35 \text{ nm}^{-1}$  (i.e.,  $2.3 \text{ \AA}$ ). (C) Magnified image of (A). (D) Simulated image (thickness:  $40 \text{ nm}$ ; defocus:  $-100 \text{ nm}$ ) with the atomic model overlaid.

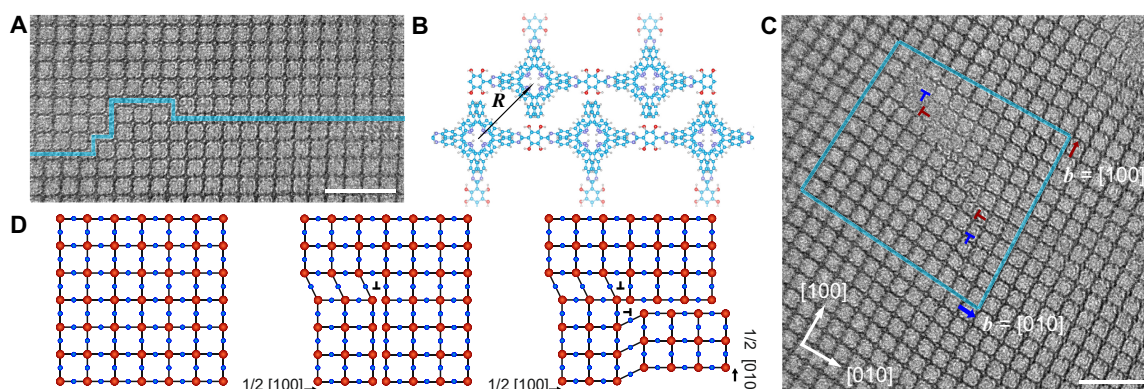


**Fig. 3. APBs visualized by AC-HRTEM imaging.** (A) APB. (B) Schematic of the APB. The arrow indicates the displacement vector  $R$ . (C) APB bounded with partial dislocations. The arrows indicate the Burgers vectors, and the partial dislocations are marked by  $\perp$ . (D) Schematic of APB formation via two nonlinear partial dislocations. The red and blue spheres represent TAPP and DhTPA units, respectively. Scale bars:  $10 \text{ nm}$ .

$$[100] \rightarrow \frac{1}{2}[100] + \frac{1}{2}[100] \text{ and } [010] \rightarrow \frac{1}{2}[010] + \frac{1}{2}[010]$$

The partial dislocation is described by the removal of either a TAPP + DhTPA plane or a pure DhTPA plane. Put differently, each partial eliminates half a unit cell. The combination of two nonlinear partials gives rise to an APB (Fig. 3D), i.e.

$$\frac{1}{2}[100] + \frac{1}{2}[010] \rightarrow \frac{1}{2}[110]$$

The APB can terminate on a second partial dislocation pair, thus restoring the perfect lattice registry or connect to GBs. Alternatively, it can form a closed loop, producing an antiphase domain encapsulated in a perfect crystal matrix (fig. S7).

Although APB has been observed in ZIF-8 (zeolitic imidazolate framework) where its origin is attributed to the oriented attachment of crystalline particles (31), suggesting possible APB formation in L-2D-PI via oriented grain coalescence, the concurrence of APBs and partial dislocations implies a disparate mechanistic explanation. As illustrated in Fig. 3D, during the polymerization, a partial dislocation can originate from a “growth error” where the DhTPA connecting two TAPPs is absent. The missing DhTPA creates an interface at which the amino groups on neighboring TAPPs adopt a head-to-head configuration. Nonetheless, on the basis of the self-assembly of porphyrin derivatives (32), such configuration introduces large

voids, leading to a decrease in surface coverage and thus an increase in surface free energy (32, 33). Consequently, the minimization of surface free energy drives the neighboring TAPPs to the antiphase sites to achieve a denser packing. We thus conclude that the APB eliminates the unfavorable interface induced by a lone partial dislocation, implementing a self-correction to the growth error.

Figure 4A presents an LAGB with a tilt angle of  $10^\circ$ . As mentioned earlier, the formation of tilt GBs is attributed to the coalescence of stochastically oriented grains. With a small tilt angle ( $<15^\circ$ ), the misorientation is accommodated by an array of edge dislocations (34). The measured dislocation spacing  $L$  is ca.  $14 \text{ nm}$ , agreeing well with the coincidence site lattice theory, i.e.,  $L = |\mathbf{b}|/2\sin(\frac{\theta}{2})$ , where  $|\mathbf{b}|$  is the size of the Burgers vector and  $\theta$  is the tilt angle (35). In the vicinity of the dislocation cores, the L-2D-PI network is subjected to local strain demonstrated by the bending of the lattice planes. The lattice distortion indicates that, despite the presence of a dislocation array, the two grains are still covalently connected across the LAGB. With increasing misorientation, however, the covalent connectivity starts to break down.

Figure 4B presents an HAGB with a tilt angle of  $28^\circ$ . Because of geometric constraints, i.e., the directionality of covalent bonding, as well as the distance and angle between the TAPPs, global covalent connectivity across the HAGB is prohibited. The HAGB can thus be described by ledges and kinks, which terminate on either TAPPs or

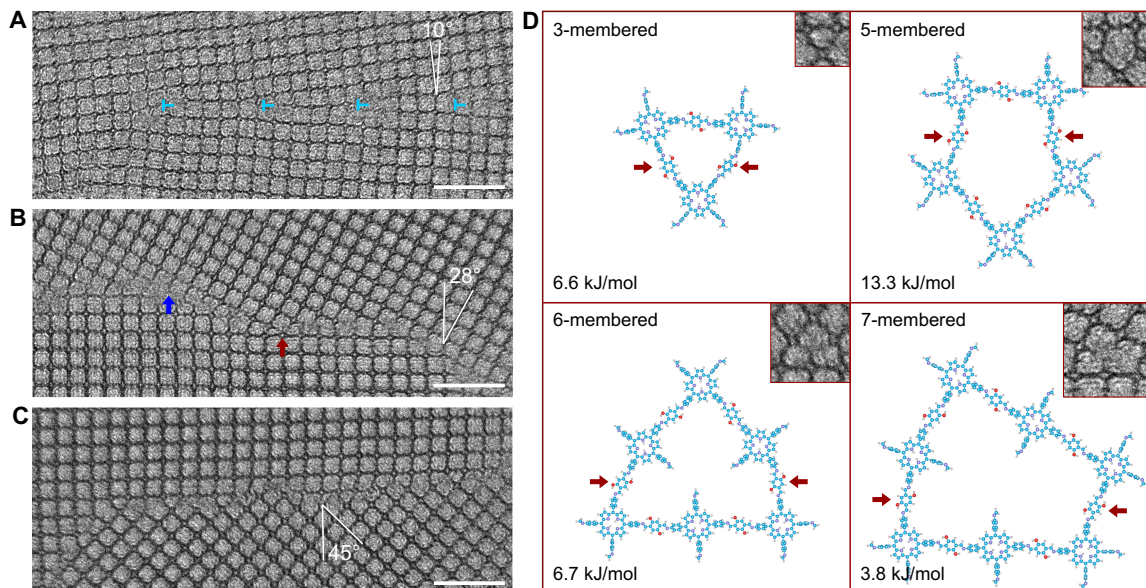


**Fig. 4. LAGB and HAGB visualized by AC-HRTEM imaging.** (A) LAGB with a misorientation of 10°. (B) HAGB with a misorientation of 28°. The red and blue arrows mark TAPP and DhTPA terminations, respectively. (C) HAGB with a misorientation of 45°. (D) DFTB models of  $n$ -membered rings formed by boundary reconstruction and the relative formation energy per inter-grain DhTPA. The red arrows mark the inter-grain DhTPAs. Scale bars: 10 nm.

dangling DhTPAs. Notably, local covalent connectivity does exist at HAGBs. Boundary reconstructions give rise to  $n$ -membered closed rings, where  $n$  refers to the number of TAPP and DhTPA units comprising the ring (i.e.,  $n$  TAPP +  $n$  DhTPA). We found 7-membered rings at the 28° HAGB (Fig. 4B) and 3-, 5-, 6-membered rings at the 45° HAGB (Fig. 4C).

Self-consistent charge (SCC)-DFTB calculations (mio-1-1 parameter set) (36) were applied to evaluate the stability of the reconstructed rings. We calculated the relative formation energy of the inter-grain DhTPAs observed in HRTEM images and compared with that in the perfect square lattice. While the standard 4-membered ring is energetically preferred, the energy penalty for creating other ring geometries is typically only a few kilojoules per mole per DhTPA (Fig. 4C), rationalizing the formation of boundary reconstructions. The validity of the ring models is further verified by a geometry optimization of an extensive section of the 45° GB (fig. S8). In all  $n$ -membered rings, the trans orientation of the imine groups as in the L-2D-PI network is energetically favorable, yet structures containing cis-oriented DhTPAs display comparable energy, indicating possible cis linkage across the GBs as well (fig. S8).

To verify whether the formation of the  $n$ -membered rings originates from the presence of the imine group, we conducted DFTB calculations with linkers containing C=C or C≡C bonds instead of imines (table S1). The energy penalty for creating the nonstandard ring geometries is comparable to or even lower than that in the L-2D-PI network, suggesting that the boundary reconstruction could be generalized to a broader group of 2D polymers.

We further studied the emergence of 3- to 7-membered rings via a general geometrical analysis at tilt GBs (Supplementary Materials). In agreement with synthesis conditions and TEM images, we assume that the edges at the GBs are chemically saturated. A similar situation has been observed and well characterized at interfaces in surface-mounted metal-organic frameworks between regions with different pore sizes (37). Sterical constraints yield a very limited

amount of low-energy ring geometries at the misoriented GBs. The 3- to 7-membered rings considered in the DFTB calculations well represent the possible ring shapes, as larger rings will have similar geometry and thus comparable formation energy. The geometrical analysis indicates that the boundary reconstruction occurs at all tilt boundaries and is not limited to the specific misorientations reported here (fig. S9 and table S2).

Because HRTEM images reveal the projected structures, it is challenging to conclude whether the boundary reconstruction is pure intralayer. Therefore, we tested the possible interlayer connection by creating a bilayer model analogous to the 3-membered ring. A set of DhTPAs was then constructed at the GB, with one DhTPA connecting the TAPPs within the same layer and one between the top and bottom layers (fig. S8). The intra- and interlayer connections are near-isoenergetic, implying the presence of both scenarios.

### GBs and mechanical stability

Because of the difficulty in resolving GB structures, the investigation of defect-property correlation in 2D polymers lags substantially behind that of their inorganic counterparts. For example, it has been reported that GBs in graphene severely weaken the mechanical strength but do not drastically change the electrical properties (17). The local photoluminescence and electrical conductivity of MoS<sub>2</sub> are strongly related to the type of GBs (18). For 2D polymers, on the other hand, the influence of GBs on material functionalities remains largely unexplored. Here, as a proof of concept, we carried out a qualitative micro-indentation test on the freestanding L-2D-PI film to investigate the correlation between GBs and mechanical stability. The micromanipulator in a focused ion beam system was used as a mechanical probe (Fig. 5A). Figure 5B presents a scanning electron microscopy (SEM) image showing the micromanipulator that is placed right above the film. After pressing L-2D-PI with the micromanipulator, the film ruptures along the GBs, which are between or inside of the micro-flowers (Fig. 5C). The decreased mechanical

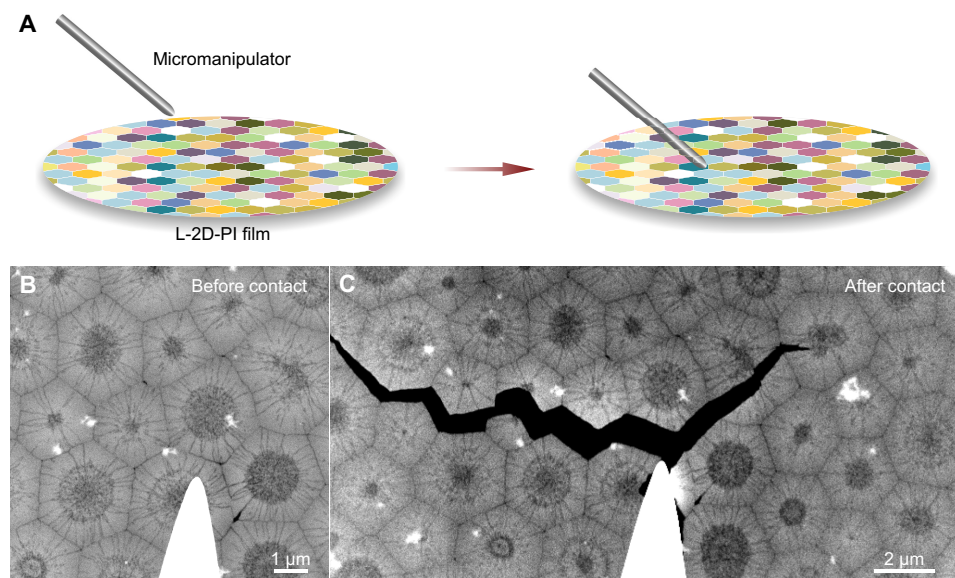


**Fig. 5. Micro-indentation of L-2D-PI.** (A) Schematic of micro-indentation. (B) SEM image of the L-2D-PI thin film. The micromanipulator of the focused ion beam system is placed right above the film. (C) After pressing the film with the micromanipulator, the film tears along GBs.

strength at GBs can be attributed to the covalent disconnections, particularly at HAGBs. This result suggests that the mechanical strength of the L-2D-PI film is dominated by its GBs. However, a quantitative determination of the mechanical strength at GBs bears further scrutiny.

## CONCLUSION

In summary, we report the direct observation of GB structures in a layer-stacked 2D polymer down to near-atomic regime. The unprocessed AC-HRTEM images are directly interpretable and free of imaging artifacts, providing unambiguous elucidation of GB structures and vital insights into GB formation mechanisms in 2D polymers. Single-crystalline grains “emanate” from specific locations, leading to the GB formation during 2D polymer growth. APBs observed in single-crystalline grains implement an energetically favorable self-correction to the missing-linker and missing-node errors. During crystal growth, LAGBs and HAGBs are formed via the coalescence of stochastically oriented grains. Covalent connectivity exists even across HAGBs, giving rise to  $n$ -membered rings via boundary reconstructions. We envisage that, with the rapid advances on the synthetic front, providing higher crystallinity, larger single crystalline grains, and more reliable intrinsic properties, the ultimate functionality of the synthetic 2D polymer thin films would be substantially affected or even dominated by the crystal defects and GBs. Although the elucidation of structure-property correlations on the microscopic level remains a formidable task, we believe that this work would lay a solid foundation for the future theoretical and experimental endeavors in the thriving field of organic 2D materials.

## MATERIALS AND METHODS

### Synthesis of L-2D-PI

L-2D-PI was synthesized in a crystallizing dish with a diameter of 5 cm and a height of 6 cm. Fifty milliliters of Milli-Q water was in-

jected into the dish, forming a static air-water interface. Then, 20  $\mu$ l of SOS (1 mg/ml in chloroform) was spread onto the interface. The solvent was allowed to evaporate for 30 min, and then TAPP (monomer 1, 0.7  $\mu$ mol in triflic acid solution) was injected into the water phase at 50°C. The monomer was allowed for dispersion in water for 1 hour, and then 2, DhTPA solution (monomer 2, 1.4  $\mu$ mol) was added to the water phase. The interfacial reaction was kept at 50°C for 5 days. TAPP was obtained from TCI Deutschland GmbH (Germany) and Porphyrin-Laboratories GmbH (Germany). DhTPA was purchased from Chem Space. SOS was purchased from Sigma-Aldrich, GmbH (Germany). All compounds were used as received.

### Transmission electron microscopy

TEM experiments were performed on an image-side aberration-corrected FEI Titan 80-300 operated at 300 kV. The microscope is equipped with a CEOS hexapole aberration-corrector that corrects the geometrical axial aberrations up to the third order. Data acquisition was conducted on a Gatan UltraScan CCD camera.

### Electron diffraction

Electron diffraction was performed in both SAED and NBED mode. For SAED acquisition, we used a selected-area aperture with a physical diameter of 50  $\mu$ m, corresponding to a diameter of 700 nm in the image plane. The total electron dose was  $2 e^-/\text{\AA}^2$  (dose rate:  $0.2 e^-/\text{\AA}^2$ ; acquisition time: 10 s). For 3D NBED, the beam diameter on the specimen was ca. 300 nm. We collected 3D electron diffraction data over 140° total tilt range (i.e.,  $\pm 70^\circ$ ) with a tilt step of 1°. The dataset was reconstructed using EDT software (AnaliteX, Sweden). For electron diffraction dose series, the total electron dose of each frame was  $4.5 e^-/\text{\AA}^2$  (dose rate:  $0.45 e^-/\text{\AA}^2$ ; acquisition time: 10 s).

### Grain imaging and orientation mapping

To examine the size, shape, and orientation of the grains, we acquired TEM images resolving up to the 200 fringe of the 25- $\text{\AA}$  unit cell (pixel size: 6.29  $\text{\AA}$ ), which allows for grain orientation mapping with nonetheless limited field of view (i.e., 1.3  $\mu$ m by 1.3  $\mu$ m). Image

stitching was then used to expand the field of view while maintaining the same CCD sampling. Consecutive images were acquired by laterally moving the sample stage by 0.8  $\mu\text{m}$ , guaranteeing  $\sim 40\%$  overlap between neighboring frames. We stitched the TEM images using cross-correlation algorithm. Grain orientation mapping was carried out on the stitched TEM image as follows: A color-coded Fourier mask was placed on the 100 ring of the fast Fourier transform (FFT) pattern (because of the fourfold symmetry, only a quadrant of the Fourier mask is shown; Fig. 1E, inset), and an inverse Fourier transform was conducted subsequently. We selected 45 orientations (i.e., 45 colors), together with the fourfold symmetry of L-2D-PI, and the angular precision was  $2^\circ$  (i.e.,  $\frac{360^\circ}{45 \times 4} = 2^\circ$ ). The average grain size on pistils was estimated from the half-width of the 100 ring on the FFT pattern. The grain sizes on petals and tilt angles at GBs were determined directly from the orientation map.

### AC-HRTEM imaging

AC-HRTEM imaging is divided into three steps, i.e., search, focus, and acquisition. Throughout the experiment, the pre-specimen shutter was applied, which automatically blanks the electron beam when CCD viewing is deactivated. To search for a point of interest while preventing irradiation damage, we selected a dose rate of  $0.2 \text{ e}^-/\text{\AA}^2\text{s}$ . The largest possible pixel size of  $108 \text{ \AA}$  was used to maximize the number of electrons per pixel. We further enhanced the contrast by bright-field TEM imaging with the smallest objective aperture (physical diameter:  $10 \mu\text{m}$ ; cutoff frequency:  $1.5 \text{ nm}^{-1}$ ). After finding a point of interest, we removed the objective aperture and configured the imaging conditions (i.e., magnification, beam intensity, etc.) for focus and acquisition while keeping the beam blanked. We chose a pixel size of  $1.15 \text{ \AA}$ , allowing information transfer to  $2.30 \text{ \AA}$ . The electron dose rate was  $500 \text{ e}^-/\text{\AA}^2\text{s}$ , and the beam diameter was  $350 \text{ nm}$ . For focus, the specimen stage was laterally shifted by  $500 \text{ nm}$  to avoid pre-exposure on the point of interest. After tuning the defocus to ca.  $-100 \text{ nm}$  (judged by the Thon rings in FFT after amorphization of the 2D polymer film within the field of view), we moved back to the point of interest and acquired a single image with a total electron dose of  $100 \text{ e}^-/\text{\AA}^2$  (dose rate:  $500 \text{ e}^-/\text{\AA}^2\text{s}$ ; acquisition time:  $0.2 \text{ s}$ ). HRTEM image simulation was carried out using QSTEM software.

### Optical microscopy, AFM, and Raman and Fourier transform infrared spectroscopy

L-2D-PI thin film was horizontally transferred onto a  $300\text{-nm SiO}_2/\text{Si}$  substrate for microscopic and spectroscopic measurements. Optical microscopy was conducted in differential interference mode with Axio Scope A1, Zeiss. AFM was performed on a customized Ntegra Aura/Spectra from NT-MDT (Moscow, Russia) with a SMENA head operated in contact mode. The Raman spectrum was excited by a  $532\text{-nm}$  ( $2.33 \text{ eV}$ ) laser. The spot size of the laser beam was ca.  $0.5 \mu\text{m}$ . Fourier transform infrared spectroscopy was performed on Tensor II (Bruker) with an attenuated total reflection unit.

### Grazing-incidence wide-angle x-ray scattering

GIWAXS measurements were carried out to examine the crystal orientation and unit cell parameters of L-2D-PI. The experiment was performed at the X-ray diffraction 1 beamline at ELETTRA, Trieste, Italy. The detector was a Dectris Pilatus 2M, and the photon beam energy was  $12.398 \text{ keV}$  ( $\lambda = 1 \text{ \AA}$ ). The sample-to-detector distance was  $349.8 \text{ mm}$  and was verified using a lanthanum hexaboride ( $\text{LaB}_6$ ) calibration standard. The grazing-incidence angle  $\alpha_i$  was

chosen to be  $0.13^\circ$ , and the sample was exposed for  $300 \text{ s}$ . The scattering data were then analyzed with WxDiff.

### DFTB calculations

Structural simulations were conducted by using the SCC-DFTB (36) as implemented in the Amsterdam Density Functional (ADF)-DFTB 2017 program suite ([www.scm.com](http://www.scm.com)). The mio-1-1 parameter set for the X-Y element pair interaction (X, Y = C, H, N, O) was used.

The periodic model of L-2D-PI was obtained using full structural optimization including the unit cell shape and volume. The trans orientation of imine groups in the DhTPAs results in a collective rotation of the TAPP units (Fig. 1B), giving rise to two configurations of stacking, i.e., in-phase and out-of-phase configurations (fig. S2). Both stacking models were refined in a 2D bilayer model, which was then transformed into a bulk structure with two layers per unit cell.

The formation of 3-, 5-, 6-, and 7-membered rings on the GBs was investigated using cluster models based on the HRTEM images shown in Fig. 4. All remaining linking sites on porphyrin cores were terminated with a 4-N-methylethaniline group to conserve the rotated structure of porphyrin cores observed in the periodic polymer structure. The validity of the cluster models was verified by a geometry optimization of a larger section of the GB based on the boundary structure with a misorientation of  $45^\circ$  (fig. S8). A universal force field (UFF) as implemented in the ADF-UFF 2017 program suite with default parameters was used for the calculation. The stabilities of the rings were compared in terms of relative reaction energy for the formation of inter-grain DhTPAs. Thus, all ring models can be compared, despite having a different number of atoms. Furthermore, all species on the reaction route were fully optimized to simulate the local geometry changes seen in the large boundary model (fig. S8).

### SUPPLEMENTARY MATERIALS

Supplementary material for this article is available at <http://advances.sciencemag.org/cgi/content/full/6/33/eabb5976/DC1>

### REFERENCES AND NOTES

1. K. S. Novoselov, A. Mishchenko, A. Carvalho, A. H. Castro Neto, 2D materials and van der Waals heterostructures. *Science* **353**, aac9439 (2016).
2. A. J. Mannix, B. Kiraly, M. C. Hersam, N. P. Guisinger, Synthesis and chemistry of elemental 2D materials. *Nat. Rev. Chem.* **1**, 14 (2017).
3. V. Georgakilas, M. Otyepka, A. B. Bourlino, V. Chandra, N. Kim, K. C. Kemp, P. Hobza, R. Zboril, K. S. Kim, Functionalization of graphene: Covalent and non-covalent approaches, derivatives and applications. *Chem. Rev.* **112**, 6156–6214 (2012).
4. H. Wang, H. Yuan, S. Sae Hong, Y. Li, Y. Cui, Physical and chemical tuning of two-dimensional transition metal dichalcogenides. *Chem. Soc. Rev.* **44**, 2664–2680 (2015).
5. P. Kissel, D. J. Murray, W. J. Wulfange, V. J. Catalano, B. T. King, A nanoporous two-dimensional polymer by single-crystal-to-single-crystal photopolymerization. *Nat. Chem.* **6**, 774–778 (2014).
6. M. J. Kory, M. Wörle, T. Weber, P. Payamyar, S. W. van de Poll, J. Dshemuchadse, N. Trapp, A. D. Schlüter, Gram-scale synthesis of two-dimensional polymer crystals and their structure analysis by x-ray diffraction. *Nat. Chem.* **6**, 779–784 (2014).
7. D. J. Murray, D. D. Patterson, P. Payamyar, R. Bhola, W. Song, M. Lackinger, A. D. Schlüter, B. T. King, Large area synthesis of a nanoporous two-dimensional polymer at the air/water interface. *J. Am. Chem. Soc.* **137**, 3450–3453 (2015).
8. K. Liu, H. Qi, R. Dong, R. Shivhare, M. Addicoat, T. Zhang, H. Sahabudeen, T. Heine, S. Mannsfeld, U. Kaiser, Z. Zheng, X. Feng, On-water surface synthesis of crystalline, few-layer two-dimensional polymers assisted by surfactant monolayers. *Nat. Chem.* **11**, 994–1000 (2019).
9. T. Zhang, H. Qi, Z. Liao, Z. Horev, L. Panes-Ruiz, P. S. Petkov, Z. Zhang, R. Shivhare, P. Zhang, K. Liu, V. Bezugly, S. Liu, Z. Zheng, S. Mannsfeld, T. Heine, G. Cuniberti, H. Haick, E. Zschech, U. Kaiser, R. Dong, F. Xinliang, Engineering crystalline quasi-two-dimensional polyaniline thin film with enhanced electrical and chemiresistive sensing performances. *Nat. Commun.* **10**, 4225 (2019).

10. Y. Zhong, B. Cheng, C. Park, A. Ray, S. Brown, F. Mujid, J.-U. Lee, H. Zhou, J. Suh, K.-H. Lee, A. J. Mannix, K. Kang, S. J. Sibener, D. A. Muller, J. Park, Wafer-scale synthesis of monolayer two-dimensional porphyrin polymers for hybrid superlattices. *Science* **366**, 1379–1384 (2019).
11. A. M. Evans, L. R. Parent, N. C. Flanders, R. P. Bisbey, E. Vitaku, M. S. Kirschner, R. D. Schaller, L. X. Chen, N. C. Gianneschi, W. R. Dichtel, Seeded growth of single-crystal two-dimensional covalent organic frameworks. *Science* **361**, 52–57 (2018).
12. M. Matsumoto, L. Valentino, G. M. Stiehl, H. B. Balch, A. R. Corcos, F. Wang, D. C. Ralph, B. J. Mariñas, W. R. Dichtel, Lewis-acid-catalyzed interfacial polymerization of covalent organic framework films. *Chem* **4**, 308–317 (2018).
13. M. S. Lohse, T. Bein, Covalent organic frameworks: Structures, synthesis, and applications. *Adv. Funct. Mater.* **28**, 1705553 (2018).
14. S. J. Lyle, P. J. Waller, O. M. Yaghi, Covalent organic frameworks: Organic chemistry extended into two and three dimensions. *Trends Chem.* **1**, 172–184 (2019).
15. M. Servalli, A. D. Schlüter, Synthetic two-dimensional polymers. *Annu. Rev. Mat. Res.* **47**, 361–389 (2017).
16. X. Feng, A. D. Schlüter, Towards macroscopic crystalline 2D polymers. *Angew. Chemie Int. Ed. Engl.* **57**, 13748–13763 (2018).
17. P. Y. Huang, C. S. Ruiz-vargas, A. M. Van Der Zande, W. S. Whitney, M. P. Levendorf, J. W. Kevek, S. Garg, J. S. Alden, C. J. Hustedt, Y. Zhu, J. Park, P. L. McEuen, D. A. Muller, Grains and grain boundaries in single-layer graphene atomic patchwork quilts. *Nature* **469**, 389–392 (2011).
18. A. M. van der Zande, P. Y. Huang, D. A. Chenet, T. C. Berkelbach, Y. You, G.-H. Lee, T. F. Heinz, D. R. Reichman, D. A. Muller, J. C. Hone, Grains and grain boundaries in highly crystalline monolayer molybdenum disulphide. *Nat. Mater.* **12**, 554–561 (2013).
19. D. Zhang, Y. Zhu, X. Ying, C.-E. Hsiung, R. Sougrat, K. Li, Y. Han, Atomic-resolution transmission electron microscopy of electron beam-sensitive crystalline materials. *Science* **359**, 675–679 (2018).
20. M. Linck, P. Hartel, S. Uhlemann, F. Kahl, H. Müller, J. Zach, M. Haider, M. Niestad, M. Bischoff, J. Biskupek, Z. Lee, T. Lehnert, F. Börrnert, H. Rose, U. Kaiser, Chromatic aberration correction for atomic resolution TEM imaging from 20 to 80 kV. *Phys. Rev. Lett.* **117**, 76101 (2016).
21. S. T. Skowron, T. W. Chamberlain, J. Biskupek, U. Kaiser, E. Besley, A. N. Khlobystov, Chemical reactions of molecules promoted and simultaneously imaged by the electron beam in transmission electron microscopy. *Acc. Chem. Res.* **50**, 1797–1807 (2017).
22. F. Haase, E. Troschke, G. Savasci, T. Banerjee, V. Duppel, S. Dörfler, M. M. J. Grunde, A. M. Burow, C. Ochsensfeld, S. Kaskel, B. V. Lotsch, Topochemical conversion of an imine into a thiazole-linked covalent organic framework enabling real structure analysis. *Nat. Commun.* **9**, 2600 (2018).
23. H. Sahabudeen, H. Qi, M. Ballabio, M. Položij, S. Olthof, R. Shivhare, Y. Jing, S. W. Park, K. Liu, T. Zhang, J. Ma, B. Rellinghaus, S. Mannsfeld, T. Heine, M. Bonn, E. Cánovas, Z. Zheng, U. Kaiser, R. Dong, X. Feng, Highly crystalline and semiconducting imine-based two-dimensional polymers enabled by interfacial synthesis. *Angew. Chemie Int. Ed. Engl.* **59**, 6028–6036 (2020).
24. R. Lacmann, A. Herden, C. Mayer, Kinetics of nucleation and crystal growth. *Chem. Eng. Technol.* **22**, 279–289 (1999).
25. J. R. Fryer, C. H. McConnell, D. L. Dorset, F. Zemlin, E. Zeitler, High resolution electron microscopy of molecular crystals. IV. Paraffins and their solid solutions. *Proc. R. Soc. Lond. A* **453**, 1929–1946 (1997).
26. Z. Lee, H. Rose, O. Lehtinen, J. Biskupek, U. Kaiser, Electron dose dependence of signal-to-noise ratio, atom contrast and resolution in transmission electron microscope images. *Ultramicroscopy* **145**, 3–12 (2014).
27. E. Spiecker, M. Garbrecht, W. Jäger, K. Tillmann, Advantages of aberration correction for HRTEM investigation of complex layer compounds. *J. Microsc.* **237**, 341–346 (2010).
28. F. Börrnert, U. Kaiser, Chromatic- and geometric-aberration-corrected TEM imaging at 80 kV and 20 kV. *Phys. Rev. A* **98**, 23861 (2018).
29. M. Wolf, D. J. DeRosier, N. Grigorieff, Ewald sphere correction for single-particle electron microscopy. *Ultramicroscopy* **106**, 376–382 (2006).
30. C. J. Russo, R. Henderson, Ewald sphere correction using a single side-band image processing algorithm. *Ultramicroscopy* **187**, 26–33 (2018).
31. Y. Zhu, J. Ciston, B. Zheng, X. Miao, C. Czarnik, Y. Pan, R. Sougrat, Z. Lai, C.-E. Hsiung, K. Yao, I. Pinnau, M. Pan, Y. Han, Unravelling surface and interfacial structures of a metal–organic framework by transmission electron microscopy. *Nat. Mater.* **16**, 532–536 (2017).
32. S. B. Lei, C. Wang, S. X. Yin, H. N. Wang, F. Xi, H. W. Liu, B. Xu, L. J. Wan, C. L. Bai, Surface stabilized porphyrin and phthalocyanine two-dimensional network connected by hydrogen bonds. *J. Phys. Chem. B* **105**, 10838–10841 (2001).
33. S. De Feyter, F. C. De Schryver, Two-dimensional supramolecular self-assembly probed by scanning tunneling microscopy. *Chem. Soc. Rev.* **32**, 139–150 (2003).
34. D. Hull, D. J. Bacon, *Introduction to Dislocations* (Elsevier, ed. 5, 2011).
35. P. Lejcek, *Grain Boundary Segregation in Metals* (Springer Berlin Heidelberg, 2010).
36. M. Elstner, D. Porezag, G. Jungnickel, J. Elsner, M. Haugk, T. Frauenheim, S. Suhai, G. Seifert, Self-consistent-charge density-functional tight-binding method for simulations of complex materials properties. *Phys. Rev. B* **58**, 7260–7268 (1998).
37. Z. Wang, J. Liu, B. Lukose, Z. Gu, P. G. Weidler, H. Gliemann, T. Heine, C. Wöll, Nanoporous designer solids with huge lattice constant gradients: Multiheteroepitaxy of metal-organic frameworks. *Nano Lett.* **14**, 1526–1529 (2014).

#### Acknowledgments

**Funding:** H.Q., B.L., T.E.G., M.M., and U.K. acknowledge the financial support from the German Research Foundation (DFG) and the Ministry of Science, Research and the Arts (MWK) of Baden-Wuerttemberg in the framework of the “SALVE” (Sub-Angstrom Low-Voltage Electron Microscopy) project (DFG KA 1295/21-1) and the EU Graphene Flagship. T.E.G. and U.K. also appreciate the DFG CRC 1279 project for financial support. H.S., S.P., R.D., and X.F. acknowledge the financial support from the ERC Consolidator Grant on T2DCP (no. 819698), the ERC Starting Grant on FC2DMOF (no. 852909), the EU Graphene Flagship (no. 785219), the COORNET (SPP 1928), the DFG project (2D polyanilines, no. 426572620), the CONJUGATION-706082, as well as the German Science Council, Center for Advancing Electronics Dresden (cfaed), EXC1056, and OR 349/1. M.P. and T.H. thank the ZIH Dresden for computer time. M.P. also thanks the financial support from the Alexander von Humboldt Foundation. M.A.A. thanks the Materials Chemistry Consortium for computational resources (EP/P020194). M.H. and S.C.B.M. acknowledge support from the German Excellence Initiative via the Cluster of Excellence EXC 1056 cfaed. The research leading to this result has been supported by the project CALIPSOplus under the Grant Agreement 730872 from the EU Framework Programme for Research and Innovation HORIZON 2020. B.V.L. acknowledges support from the Cluster of Excellence “e-conversion” and an ERC Starting Grant (COFLeaf, grant no. 639233). Z.Z. thanks the financial support from the National Natural Science Foundation of China (51873236 and 51833011) and the Youth 1000 Talent Program of China. R.D., T.H., X.F. and U.K. acknowledge the funding from the DFG in SFB-1415 (no. 417590517). **Author contributions:** X.F. and R.D. conceived and designed the 2D polymer synthesis approach. H.Q. designed and performed the TEM experiments under the guidance of U.K. H.S. synthesized the 2D polymer and performed Raman and FT-IR spectroscopy. H.Q., B.L., T.E.G., M.M., B.V.L., and U.K. analyzed and/or discussed the TEM data. M.P., M.A.A., and T.H. performed the DFTB calculations and analyzed the data. T.E.G. performed the 3D diffraction experiment. M.H. and S.C.B.M. conducted the GIWAXS measurements and analyzed the data. M.M. carried out the micro-indentation test. S.P. conducted the AFM measurement. H.S., Z.Z., R.D., and X.F. proposed the reaction mechanism concept. H.Q. and U.K. wrote the manuscript, with major contributions from H.S., M.P., and R.D. and extended comments from T.H. and X.F. All authors commented on the manuscript. **Competing interests:** The authors declare that they have no competing interests. **Data and materials availability:** All data needed to evaluate the conclusions in the paper are present in the paper and/or the Supplementary Materials. Additional data related to this paper may be requested from the corresponding authors.

Submitted 5 March 2020

Accepted 1 July 2020

Published 14 August 2020

10.1126/sciadv.abb5976

**Citation:** H. Qi, H. Sahabudeen, B. Liang, M. Položij, M. A. Addicoat, T. E. Gorelik, M. Hamsch, M. Mundsinger, S. Park, B. V. Lotsch, S. C. B. Mannsfeld, Z. Zheng, R. Dong, T. Heine, X. Feng, U. Kaiser, Near-atomic-scale observation of grain boundaries in a layer-stacked two-dimensional polymer. *Sci. Adv.* **6**, eabb5976 (2020).